Visual Knowledge Discovery for Diffusion Kurtosis Datasets of the Human Brain

Sujal Bista, Jiachen Zhuo, Rao P. Gullapalli, Amitabh Varshney

Abstract Classification and visualization of structures in the human brain provide vital information to physicians who examine patients suffering from brain diseases and injuries. In particular, this information is used to recommend treatment to prevent further degeneration of the brain. Diffusion kurtosis imaging (DKI) is a new kind of magnetic resonance imaging rapidly gaining broad interest in the medical imaging community due to its ability to provide intricate details of the underlying microstructural characteristics of the whole brain. DKI produces a fourth-order tensor at every voxel of the imaged volume; unlike traditional diffusion tensor imaging (DTI), DKI measures the non-Gaussian property of water diffusion in biological tissues. It has shown promising results in studies on changes in grey matter and mild traumatic brain injury, a particularly difficult form of TBI to diagnose. In this paper, we use DKI imaging and report our results of the classification and visualization of various tissue types, diseases, and injuries. We evaluate segmentation performed using various clustering algorithms on different segmentation strategies including fusion of diffusion and kurtosis tensors. We compare our result to the well-known MRI segmentation technique based on Magnetization-Prepared Rapid Acquisition with Gradient Echo (MPRAGE) imaging.

Sujal Bista
Institute for Advanced Computer Studies, University of Maryland, College Park, MD, 20742, USA
e-mail: sujal@umiacs.umd.edu

Jiachen Zhuo
University of Maryland School of Medicine, Baltimore, MD, 21201, USA e-mail: jzhuo@umm.edu

Rao P. Gullapalli
University of Maryland School of Medicine, Baltimore, MD, 21201, USA e-mail: rgullapalli@umm.edu

Amitabh Varshney
Department of Computer Science and Institute for Advanced Computer Studies, University of Maryland, College Park, MD 20742, USA e-mail: varshney@cs.umd.edu

1 Introduction

Traumatic brain injury (TBI), caused by blows to the head, is a leading cause of death and disabilities. In 2010, in the United States alone, TBI resulted in 2.5 million hospitalizations and 50,000 deaths [5]; Survivors often face lifelong disabilities. Medical professionals examine, diagnose, and treat these injuries; once injury occurs, a major focus is on how to prevent further extensive degeneration of the brain. The examination can significantly impact recovery, as subsequent diagnosis and treatment depend on it. Different types of medical imaging modalities, including magnetic resonance imaging (MRI) , are used for examining TBI injuries.

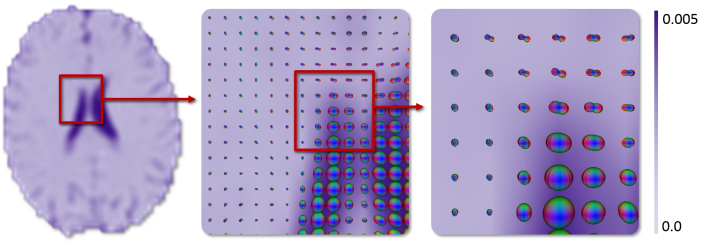

(a) Diffusion Tensor

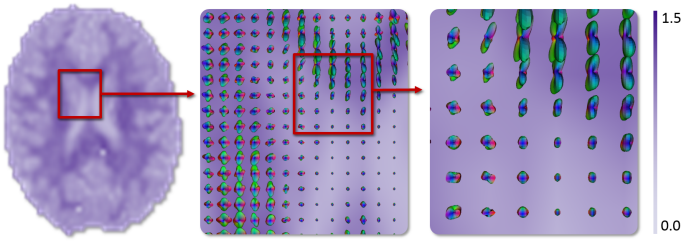

(b) Kurtosis Tensor

Fig. 1 The diffusion tensor (DT) and kurtosis tensors (KT) visualized using glyph overlays. Each shape shows properties of the underlying tissue. The diffusion values are high and isotropic in the cerebral spinal fluid (CSF) and gray matter (GM) regions, whereas they are low and anisotropic in the white matter (WM). The kurtosis values are high around the injury and the WM region.

MRI is a non-invasive imaging device that uses powerful magnetic fields to image the diffusion patterns in biological tissues. Diffusion Tensor Imaging (DTI) is an increasingly popular MRI technique that detects diffusion of water to infer underlying tissue microstructure. DTI assumes that the water diffusion patterns follow a Gaussian distribution; it can effectively measure the dominant direction of water diffusion in tissues, and is widely used in studying white matter tracts in the brain. However, the Gaussian distribution assumption of the DTI fails whenever diffusion is restricted by injury or diseases. To address this problem, Jensen and Helpern [15]

introduced diffusion kurtosis imaging (DKI) , which measures the degree of the diffusional non-Gaussianity of water molecules in biological tissues. DKI has gained attention in the medical imaging community because of its ability to show a more detailed structure of underlying tissues and because it shows promise in detecting micro-structural tissue changes caused by mild traumatic brain injuries and other neurological diseases [43]. In DKI, second-order diffusion tensors (DT) and fourth-order kurtosis tensors (KT) are calculated. These tensors are spatio-angular fields that characterize the underlying imaged tissue, as shown in Figure 1. Both DT and KT capture properties of underlying tissues that can be used to classify the whole brain by different tissue types. In both of these datasets, each sample point can be represented by a unique shape defined by its directional data. The per-sample shape of a spatio-angular field in KT is highly irregular and complicated compared with the DT, because KT is capable of estimating finer properties of the imaged tissue.

Classification and visualization of structures in the human brain provides vital information to medical professionals examining patients who suffer from brain diseases and injuries. Detailed information on the imaged tissues can help these professionals decide what actions to take to prevent further degeneration of the brain. Tissue segmentation is also important in studying the structure and function of the brain. There are numerous medical literature reviews that detail the classification of the brains structure , fusing data from either single or multiple imaging techniques, such as DTI and high-angular-resolution diffusion imaging (HARDI) [12, 24, 29, 28, 33, 34]. Most methods rely on utilizing a statistical summarization of the datasets, such as the mean value, by identifying appropriate ranges of various tissue types. This requires systematic domain knowledge and is error-prone because initial tissue selection used for training determines the quality of the output of classification. Also, it is difficult to find tissues for rare diseases. To our knowledge, no work has been done that performs segmentation by fusing the per-sample shapes of Gaussian and non-Gaussian diffusion estimated by diffusion and kurtosis tensors in DKI. In this paper, we report our classification and visualization results from DKI tensors based on tissue types, diseases, and injuries. We evaluate different segmentation strategies, and compare them to the latest MRI segmentation technique based on magnetization prepared rapid acquisition with gradient echo (MPRAGE) imaging. We also carry out efficient visualization of these segments using spherical harmonics lighting functions, to facilitate insights into the micro-structural properties of the imaged tissue volume.

2 Related Work

Numerous studies and literature reviews have been conducted on the segmentation and visualization of brain tissues using various types of MRI.

Prckovska *et al.* [34] use high angular resolution diffusion imaging anisotropy measures to classify different diffusion models (isotropic, Gaussian, and non-Gaussian). Their approach requires an estimation of threshold intervals to perform classification, which can be complex and requires a advanced level of domain knowledge.

In another study, Prckovska *et al.* [33] perform semi-automatic human-assisted classification of diffusion structures to separate different diffusion models, such as isotropic, anisotropic Gaussian, and non-Gaussian areas. A domain expert selects regions for all three different tissue types. Then the distribution is calculated and used to perform segmentation. Researchers also introduce a hybrid approach to visualize the structure of diffusion. Ellipsoids are used to display a simple diffusion shape, and ray-traced spherical harmonics glyphs display the complex structures based on the segmentation result.

Hasan *et al.* [12] use DTI to segment and partition cerebrospinal fluid (CSF) , grey matter (GM) , and white matter (WM) . In their method, domain experts manually select 50 regions-of-interest for each tissue type. These regions are then used to create a tissue classification threshold used in a multidimensional supervised clustering procedure to segment the whole brain into three tissue types.

Lui *et al.* [28] use multiple domain-based attributes, such as the apparent diffusion coefficient and fractional anisotropy, to automatically segment CSF, GM, and WM. The apparent diffusion coefficient and eigenvectors from the diffusion tensor are used to separate CSF from other regions, such as GM and WM, then the fractional anisotropy value is employed to separate GM and WM. An expectation-maximization algorithm combined with a hidden Markov random field model is used to perform automatic segmentation.

Recently, constrained spherical deconvolution has been deployed on diffusion-weighted datasets to classify various tissue types and find fiber-track orientations [18, 35]. Jeurissen *et al.* [18] performed constrained spherical deconvolution on multi-shell diffusion weighted data with high angular resolution. Using a multi-shell multi-tissue model, they were directly able to classify CSF, GM, and WM. In this paper, we focus on DT and KT to perform classification. These datasets are acquired using significantly lower angular resolution readings compared to other diffusion imaging techniques such as high angular resolution diffusion imaging.

A few studies have looked into the classification and visualization aspects of DKI data. Lu *et al.* [29] use the spherical harmonics basis to analyze DKI datasets. Researchers limited the harmonic analysis to three bands (0, 2, and 4) and used coefficient summation ($C0$, $C2$, and $C4$) to describe the rotationally invariant property of each band. Then WM, GM, and fiber crossings are segmented based on the fractional anisotropy and $C0$ coefficient only, where $C0$ is a directionally-averaged apparent kurtosis coefficient equivalent to the mean kurtosis. In their paper, $C0$ values were 0.74 ± 0.03, 1.09 ± 0.01, and 0.84 ± 0.02 for GM, WM, and thalamus, respectively. It is interesting to note that, in their segmentation, they did not use $C2$ and $C4$, which are associated with a higher frequency signal in the rotationally invariant

spherical harmonics coefficient. This higher frequency information has not yet been fully explored. In this paper, we classify brain tissues using the per-voxel shapes of DT and KT, which provides a better grouping of similar structures and also enhances the likelihood of detecting anomalies.

Volume rendering is widely used to visualize MRI datasets. A considerable amount of work has been done to improve visualization by incorporating advanced shading techniques, multiple depth cues, transfer functions, multiple lighting, and global illumination [6, 13, 14, 22, 23, 25, 26, 27, 30, 36, 39, 41, 42]. These studies on volume rendering contain significant ways to improve the visual quality of the volume being displayed. This work on visualization builds on our previous work [2], in which we used spherical harmonics lighting functions to facilitate a more meaningful visualization of dense spatio-angular datasets. In this work, we extend this method to support automatic segmentation and visualization of the entire brain.

3 Overview

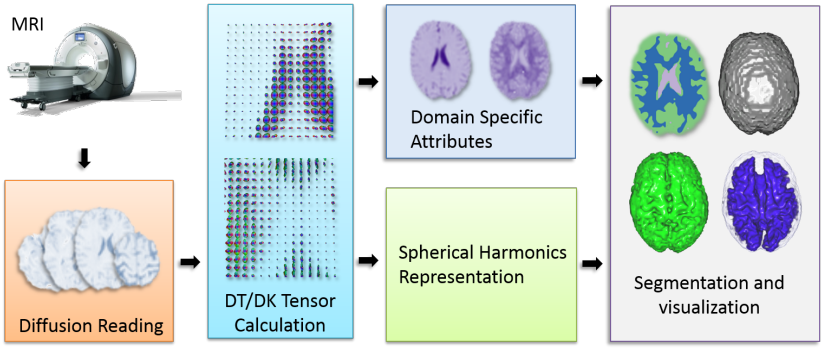

Fig. 2 An overview of our proposed method. First, a large number of diffusional readings are recorded by MRI. Then, we compute tensors and other domain-specific attributes. Next, the tensors are converted to a spherical harmonic form. After that, we use spherical harmonics approximation of DT and KT to classify various tissue types. Finally, by combining the dynamic spherical harmonics lighting functions and the segmented data, the image is rendered. The output is either a planar-rendered image, a volume-rendered image, or both.

The proposed method takes spatio-angular fields (such as DT and KT) as inputs and converts them into a spherical harmonics representation using spherical harmonics basis functions. Tissues are then classified using the spherical harmonics representation of both the DT and DK. Depending on the task and the complexity of the field, we choose to configure either single or multiple spherical harmonics lighting functions for visualization. Finally, by combining classified segments, the dynamic

spherical harmonics lighting functions, and the input spatio-angular field, we render the image. We provide two modes to view the final output using either planar or volume rendering. An overview of our approach is shown in Figure 2.

4 Background

4.1 Diffusion Tensor Imaging

DTI assumes a Gaussian diffusion process of water in the imaged tissue. The Taylor series expansion [19] is used to approximate the diffusion-weighted signal for each gradient direction, expressed by :

$$ln\left[S\left(g,b\right)\right] = ln\left[S_0\right] - bD_{app}\left(g\right) + O\left(b^2\right),$$

$$D_{app}\left(g\right) = \sum_{i=1}^{3}\sum_{j=1}^{3} g_i g_j D_{ij},$$

where g is the diffusion gradient, b is the MRI acquisition parameter b-value expressed in s/mm^2, S_0 is the signal without diffusion weighting, D_{ij} is the element of the diffusion tensor, and D_{app} is the apparent diffusion coefficient. The diffusion tensor, which is a second-order symmetric tensor with six independent elements, is calculated for each voxel. By using eigen-decomposition of the diffusion tensor we compute the dominant diffusion directions.

4.2 Diffusion Kurtosis Imaging

DKI measures the non-Gaussian property of water diffusion. The traditional DTI technique estimates the tensor, based on the assumption that water diffusion patterns follow a Gaussian distribution. This is true for longer diffusion time scales or when there are no obstructions. However measuring diffusion over shorter time periods shows the local diffusion to adhere to the tissue micro-environment. This diffusion heterogeneity gives rise to a non-Gaussian probability distribution function for water diffusion; a limitation for traditional DTI which assumes diffusion to have Gaussian distribution [16]. To measure the degree of the diffusional non-Gaussianity of water molecules in the imaged tissues, Jensen and Helpern [15] introduced DKI. Compared to DTI, data acquisition needs are much larger in DKI; the kurtosis tensor is often computed using data from 30 diffusional directions, using at least two non-zero diffusion sensitivities. Common b-values used in DKI acquisition are 0, 1000, and $2000 s/mm^2$, and the scan time can be as long as 10 min. While other forms of higher-order diffusion-weighted imaging techniques exist, such as high angular resolution diffusion imaging or diffusion spectrum imaging, they are less clinically practical because they take a considerably longer time to scan as they require a higher number of diffusional direction and b-values. The Taylor series equation in Section 4.1 is further expanded to measure the non-Gaussian property

of the water diffusion [15, 16]. A fourth-order diffusion kurtosis tensor is calculated from the diffusional measurements in DKI using the equation described by Jensen and Halpern [16],

$$ln\left[S\left(g,b\right)\right] = ln\left[S_0\right] - bD_{app}\left(g\right) + \frac{1}{6}b^2 D_{app}\left(g\right)^2 K_{app}\left(g\right) + O\left(b^3\right),$$

$$K_{app}\left(g\right) = \frac{1}{D_{app}\left(g\right)^2}\sum_{i=1}^{3}\sum_{j=1}^{3}\sum_{k=1}^{3}\sum_{l=1}^{3} g_i g_j g_k g_l K_{ijkl},$$

$$K_{ijkl} = MD^2 W_{ijkl},$$

where MD is the mean diffusivity, K_{app} is the apparent kurtosis, and W_{ijkl} is the element of kurtosis tensor. The kurtosis tensor is a symmetric fourth-order tensor with 15 independent elements. In full form, the signal in each gradient direction is described by

$$ln\left[S\left(g,b\right)\right] = ln\left[S_0\right] - b\sum_{i=1}^{3}\sum_{j=1}^{3} g_i g_j D_{ij} + \frac{1}{6}b^2\sum_{i=1}^{3}\sum_{j=1}^{3}\sum_{k=1}^{3}\sum_{l=1}^{3} g_i g_j g_k g_l K_{ijkl},$$

4.3 Spherical Harmonics

We approximate DT and KT using spherical harmonics basis functions that are later used for classification and visualization. Spherical harmonics are basis functions used to represent and reconstruct any function on the surface of a unit sphere. Spherical harmonics are defined over the surface of a sphere in the same way Fourier functions are defined on a circle [32]. In computer graphics and visualization, spherical harmonics are used for lighting scenes with low frequency lights, for subsurface scattering, and for global illumination, because they can inexpensively approximate a computationally-complex physical process [4, 20, 10, 36, 37, 38, 42].

Spherical harmonics are ortho-normal functions defined by

$$Y_l^m(\theta,\phi) = (-1)^m\sqrt{\frac{2l+1}{4\pi}\frac{(l-m)!}{(l+m)!}}P_l^m(\cos\theta)e^{im\phi},$$

where l is the band index, m is the order, P_l^m is an associated Legendre polynomial, and (θ,ϕ) is the representation of the direction vector in the spherical coordinate. We use real-valued spherical harmonics because the values used to define spatio-angular fields are positive and real.

To convert the function $f(\theta,\phi)$ into a spherical harmonics basis, spherical harmonics coefficients a_l^m are approximated using the equation

$$a_l^m = \int_s f(\theta,\phi)Y_l^m(\theta,\phi)ds,$$

A benefit of using spherical harmonics representation is that integrating two functions over the sphere can be estimated in an inexpensive way by performing a dot product of their spherical harmonics coefficients [3, 20].

$$\int U(s) \times V(s) ds = \sum_{i=0}^{l^2} u_i(s) \times v_i(s),$$

where U and V are two functions defined on the surface of a sphere, and $u(s)$ and $v(s)$ are their spherical harmonics coefficients.

5 Image Acquisition and Pre-processing

The 3T Siemens Tim Trio Scanner (Siemens Medical Solutions; Erlangen, Germany) was used to perform imaging. Diffusion weighted images were obtained with $b = 1000, 2000 s/mm^2$ in 30 directions, together with 4 b_0 images, in-plane resolution $= 2.7 mm^2$, echo time/time repetition $= 101 ms/6000 ms$ at a slice thickness of $2.7 mm$ with two averages. DKI reconstruction was carried out on each voxel using a MATLAB program, as described by Zhuo *et al.* [43]. There are also newer alternative methods for computing kurtosis tensors by Ghosh *et al.* [9] and Tax *et al.* [40].

Once diffusion and kurtosis tensors are computed, we represent the shape of these tensors by using spherical harmonics approximation. From the diffusion and the kurtosis tensors, we use D_{app} and K_{app} to compute the shapes of Gaussian and non-Gaussian diffusion. Each shape is then represented in the spherical harmonics basis by computing spherical harmonics coefficients a_l^m. Based on the complexity of the shape, the number of coefficients used in spherical harmonics representation varies. The shape of the diffusion tensor is simpler than the kurtosis tensor. As described by Lu *et al.* [29], we used bands 1, 3, and 5 to represent the shape of the symmetric kurtosis tensor. This can be done using 15 spherical harmonics coefficients (there are 25 coefficients in total, but bands 2 and 4 are not used). Bands (> 5) can be used too; however, high frequency data contains more noise, as discussed in [29]. These spherical harmonics coefficients capture the shape, magnitude, and direction of the tensors, which are used for segmentation and visualization.

5.1 Classification Reference Datasets

To compare various classification approaches, we perform tissue classification using $3D\ T1$-weighted MPRAGE images, which is commonly used for brain tissue segmentation. These images were segmented to CSF, GM and WM using the SPM8 software package [1], and they served as the ground truth. The tissue masks were then aligned and under sampled to the DKI space through co-registration of the frac-

tional ansiotropy map and the WM tissue probability map, also through SPM8. As an initial step, we classify the DKI derived maps to different tissue types. It should be noted that T1-weighted MPRAGE images may not always be available, and that the image distortion inherent in diffusion weighted image may have an effect on co-registration, leading to inaccurate tissue classification. We demonstrate a method that can classify the tissue type reliably based on the DKI data.

6 Classification

Classifying spherical harmonics volume fields into smaller sub-regions is beneficial for both visualization and analysis. Local features can be enhanced or suppressed as desired, lighting functions can be optimized if the classification captures complexity of the spherical harmonics field, and grouping simplifies the analysis process because it can reflect domain-specific information. While there are several ways to accomplish segmentation in volume rendering, a popular method is to examine the intensity-gradient histogram to find the edge boundaries in order to segment different regions. In practice, there are different types of soft tissues in an image, and the boundaries may not be clearly defined. Instead of scalar values, our dataset contains irregular multi-dimensional geometric shapes. Furthermore, these datasets come with multiple attributes, which must be examined carefully in order to do the segmentation. This process can be very difficult. To classify the dataset, we examine two approaches: domain-specific classification and shape based classification.

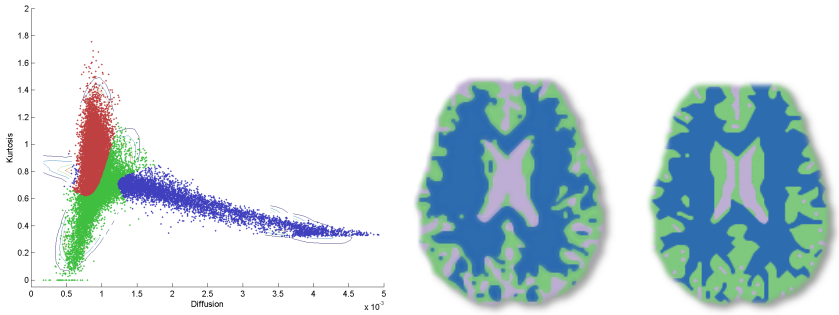

(a) (b) (c)

Fig. 3 The Gaussian mixture model is applied to mean diffusion and mean kurtosis data shown in Figure 3(a). Three means are used to classify CSF, GM, and WM. We compare segmentation performed using MPRAGE Figure 3(b) with GMM based segmentation performed using mean diffusion (MD) and mean kurtosis (MK) images Figure 3(c).

6.1 Domain specific classification

In DKI, several domain-specific attributes having biological relevance are computed. They are mean diffusion, fractional anisotropy, and mean kurtosis. To apply domain-specific classification, we apply the popular clustering algorithms K-means [11] and Gaussian mixture models (GMM) [31] on the mean kurtosis and mean diffusion. The relation between the mean diffusion and kurtosis has been explored by Jensen *et al.* [17]. They both capture properties of the imaged tissue. Here we use K-means and GMM to automatically cluster the dataset into segments. The results of GMM-based classification can be seen in Figure 3.

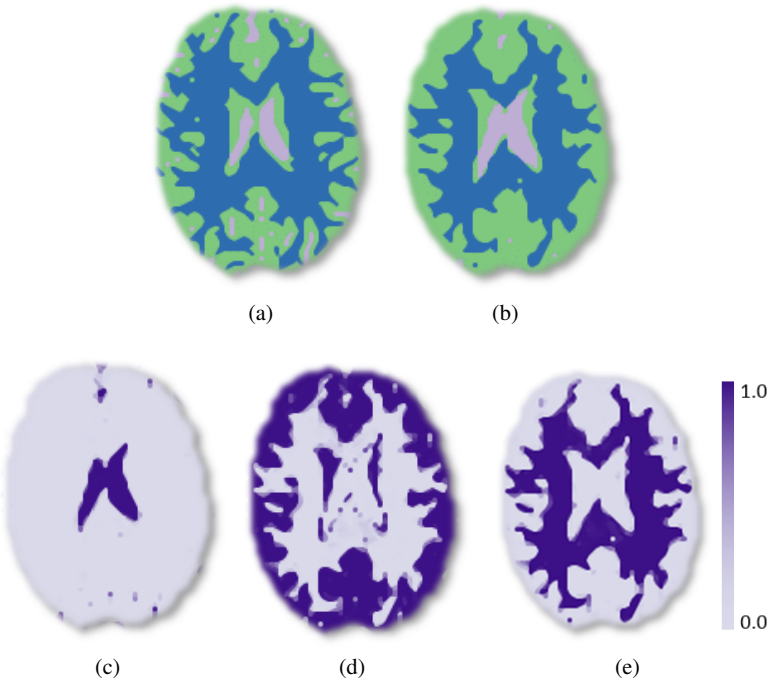

Fig. 4 We compare segmentation performed using MPRAGE image (Figure 4(a)) with segmentation performed by applying K-means (with $k = 3$) on a rotationally-invariant spherical harmonics approximation of diffusion and kurtosis tensors (Figure 4(b)). Grey, green, and blue represent CSF, GM, and WM respectively. In Figure 4(c), Figure 4(d), and Figure 4(e), we show the degree of membership of each pixel to different segments.

6.2 Shape-based classification

We use the shape of the DT/KT tensor at each voxel to perform shape based classification across the entire volume. When comparing the shape of tensors, we consider two components: structure of the tensors and their orientation. Here we focus on just the shape by using the rotationally invariant spherical harmonics form for

classification. The rotationally invariant spherical harmonics form is computed by performing the summation of all the spherical harmonic coefficients within the same band as described by [8, 21]. Coefficients of the spherical function become

$$R(f(\theta,\phi)) = \{\|f_0(\theta,\phi)\|, \|f_1(\theta,\phi)\|, ..., \|f_\infty(\theta,\phi)\|\}$$

where

$$f_l(\theta,\phi) = \sum_{m=-l}^{l} a_l^m Y_l^m(\theta,\phi)$$

Shape-based classification is a general approach that can be applied to any spatio-angular field. To categorize data into segments, clustering-based algorithms, K-means [11] and GMM are applied to the rotationally-invariant spherical harmonics attribute. The application of these clustering algorithms on shape-based attributes will group shapes together based on centroids or density. To apply these algorithms, we first adjust the rotationally invariant spherical harmonics representation of each dataset so that they are centered on the origin and have a unit standard deviation. $R_l^{'} = \frac{R_l - \mu_{\{R_0,R_1,....,R_L\}}}{\sigma_{\{R_0,R_1,....,R_L\}}}$, where L is total number of bands used. This normalization is an important step as different datasets, such as rotationally invariant spherical harmonics approximation of diffusion and kurtosis tensors, might have different data distribution. If one dataset is more compact than another, the properties of the compact dataset might not be well represented after segmentation. An extra weighting variable can also be applied depending on the need. Once the data is adjusted, we apply the clustering algorithms.

We have explored shape-based classification to segment various tissue types. For the KT dataset, we have three coefficients $(R^{'}_{0_{dk}}, R^{'}_{2_{dk}}, R^{'}_{4_{dk}})$ for each voxel from the rotationally-invariant spherical harmonics attribute. For the DT and KT dataset we have six coefficients $(R^{'}_{0_{dt}}, R^{'}_{2_{dt}}, R^{'}_{4_{dt}}, R^{'}_{0_{dk}}, R^{'}_{2_{dk}}, R^{'}_{4_{dk}})$, three coefficients each for the diffusion and kurtosis tensors. The shape of the diffusion tensor characterizes the underlying Gaussian diffusion profile, whereas the kurtosis tensor describes the non-Gaussian diffusion profile. We cluster the dataset into 3 different segments and compare the result with the tissue classification performed on an MPRAGE image based on data from 8 normal subjects. In Figure 4, we show tissue classification performed on an MPRAGE image (Figure 4(a)) along with segmentation performed by applying K-means (with $k = 3$) on the rotationally-invariant spherical harmonics approximation of the combined DT/KT dataset (Figure 4(b)). In Figure 4(c), Figure 4(d), and Figure 4(e) we show degree of membership of each pixel with its segment.

In the study by Falangola *et al.* [7], three distinct peaks for CSF, GM, and WM were observed in the MK histogram around 0.45, 0.75, and 1.25 respectively in the frontal lobe white matter. We compare segmentation result by applying the K-means algorithm (with $k = 3$) to the rotationally invariant form of the spherical harmonics approximation of diffusion and kurtosis with MPRAGE-based segmentation.

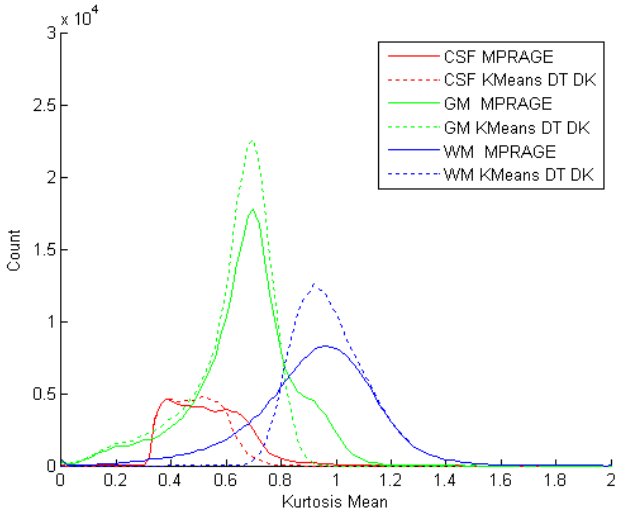

Fig. 5 Histogram plot of mean kurtosis (MK) for MPRAGE image and segmentation performed using K-means algorithm (with $k = 3$) on the rotationally invariant form of the spherical harmonics approximation of diffusion and kurtosis tensors. The peaks from both MPRAGE and the DT/KT segmentation are aligned with each other, which shows a good match between the two segmentation methods.

Segmentation Type	Classification Type	Percentage match mean	Percentage match STD
GMM on MK	Domain	61.61	02.59
GMM on MD and MK	Domain	54.55	14.71
K-means on MD and MK	Domain	61.43	02.94
GMM on RI DT/KT	Shape	68.35	16.00
K-means on RI KT	Shape	64.92	03.09
K-means on RI DT/KT	Shape	77.50	01.32

Table 1 Comparison of various segmentation methods on different data type with performance on MPRAGE image.

We apply segmentation on 8 MRIs of normal subjects and plot the combined histogram values of mean kurtosis(MK) for each segment, the results of which are shown in Figure 5. The peaks of the histogram are aligned with each other. More interestingly, the MK histogram indicates a narrow distribution of MK values of all three tissue types, reflective of likely more accurate tissue classification using the shape based method.

The full result of classification is shown in Table 1. K-means applied on combined DT and KT performs best with 77% match with the MPRAGE tissue classification. GMM produces good results when the CSF, GM, and WM have distinct density peaks. However, the distribution of each tissue type varies in each MRI and sometimes causes GMM to select a distribution that does not correspond to CSF, GM

or WM. As the K-means algorithm searches for centroids and is geometric in nature, it provided better classification compared to the other techniques because the geometric properties of the tensors are closely tied to the underlying tissue types.

	Volume Ratio					
Segmentation Type	CSF Mean	CSF STD	GM Mean	GM STD	WM Mean	WM STD
GMM on MK	0.129	0.112	0.638	0.177	0.231	0.076
GMM on MD and MK	0.244	0.064	0.408	0.230	0.347	0.240
K-means on MD and MK	0.267	0.025	0.440	0.016	0.272	0.016
GMM on RI DT/KT	0.248	0.070	0.415	0.130	0.335	0.134
K-means on RI KT	0.251	0.029	0.448	0.015	0.286	0.020
K-means on RI DT/KT	0.126	0.035	0.508	0.028	0.363	0.017
MPRAGE	0.148	0.026	0.491	0.026	0.359	0.012

Table 2 A comparison of various segmentation methods with MPRAGE based classification. Volume ratio, which is a ratio between volume occupied by a tissue and the volume of the whole brain, is calculated for each tissue type.

The volume ratio of a given tissue type is the ratio between the volume occupied by that tissue and the volume of the entire brain. We calculate the volume ratio for all three tissue types. The volume ratios of different tissue types using our shape based segmentation and MPRAGE segmentation are shown in Table 2. We compare these with the volume ratios for MRI data from healthy subjects. K-means applied on combined DT/KT performs close to the MPRAGE tissue classification. As mentioned before, when there are no distinct density peaks, the output of the GMM algorithm degrades.

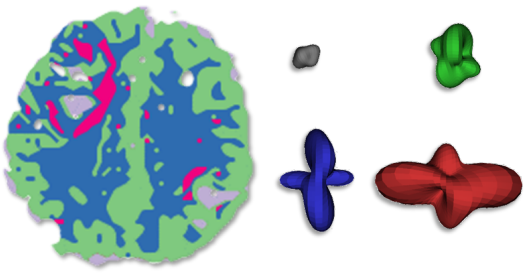

Fig. 6 Result of applying K-means (with k= 4) segmentation to differentiate CSF (grey), GM (green), and WM (blue) along with extreme kurtosis values (red). The area surrounding the injury site has very high kurtosis values. The representative DKI glyph for each segment is also shown.

6.3 Representative Shape

After classifying various segments, we compute a representative shape for each segment for analysis and lighting in visualization. We determine a representative shape

for lighting by using the mean value for each group based on attributes used for grouping. The voxel most closely representing the mean is chosen to represent the shape function. Figure 6 shows the segmentation performed on the DKI image of a patient with traumatic brain injury (TBI) using K-means (with k= 4) and the representative shape for each segment. The regions around the injury, as shown in red, have extreme kurtosis values, depicted by their elongated shapes.

7 Visualization

In a previous paper [2], we used spherical harmonics lighting functions to analyze and visualize spatio-angular fields, such as diffusion and kurtosis tensors. Dynamic spherical harmonics lighting functions, which have unique directional shapes and sizes, are used as a query tool to illuminate the spatio-angular field and visualize the underlying structure. The output of the system is either a planar visualization or a volume rendering. In this work, our system uses the same tool with added support for visualizing segmented regions.

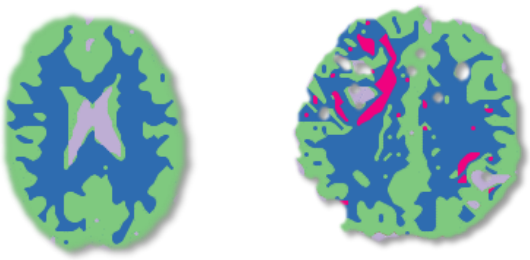

(a) (b)

Fig. 7 Shape-based classification using K-means segmentation (with $k = 3$) on the spherical harmonics approximation of diffusion and kurtosis tensors. Figure 7(a) shows segmentation into CSF (grey), WM (blue), and GM (green) on a normal subject. In Figure 7(b), we use the MRI of an injured patient. The segments show the injured region (red), WM (blue), and GM (green).

7.1 Planar Visualization

For planar visualization, we have several ways of visualizing the data. One direct way is to map segment identifiers to specific colors using a transfer function; this visualization mode allows easy identification of various segments. Although this method is straightforward, one needs to be careful in color assignment for different segment identifiers so that coloring across MRIs is consistent, as the segment identifiers from GMM or K-means can stochastically change for every run of the

algorithm. An example visualization is shown in Figure 7, comparing the MRI of a normal subject and an injured patient. For segmentation, shape-based classification using K-means segmentation (with three segments) on spherical harmonics approximations of the diffusion and kurtosis tensors is performed. Figure 7(a) shows the MRI segmentation of a normal subject, where segments relate to CSF (grey), WM (blue), and GM (green). In Figure 7(b), we use the MRI segmentation of a patient suffering from traumatic brain injury, in which segments show the injured region (red), WM (blue), and GM (green).

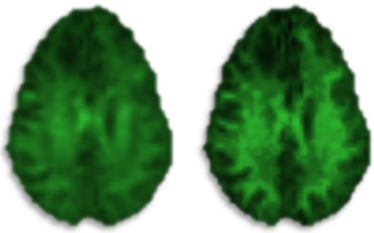

Fig. 8 The difference between lighting using a regular lighting function (left) and a local representative light (right). Using the representative glyph to light the volume field will exaggerate local differences, as seen in the second image.

7.2 Planar Visualization using Representative Shapes

The second form of planar visualization uses local shape-based lighting. In our previous work [2], lighting functions were used to illuminate spatio-angular fields to show the structural properties of the underlying tissues. The lighting functions can be modified or rotated to allow active exploration of the dataset. Most lighting functions used were pre-defined shapes. However, lighting functions do not have to be constrained to pre-defined shapes. In the previous section, we computed the representative shape for each cluster; using these shapes, each voxel can be lit by its group's representative shape, as shown in Figure 8. With this lighting, a higher value characterizes the close approximation between the shape of the spherical harmonic voxel field and its representative shape, which is similar to the degree of membership used in segmentation.

7.3 Volume Visualization of Segments

For volume visualization of the segmented data, we map the segment identifiers to color and opacity using a transfer function. After the MRI dataset is segmented, we create a scalar field using the segment identifiers. This field is used in volume rendering to perform a lookup of the transfer function. Based on the user preference, the opacity of the selected segment is increased while making other segments semi-transparent. In Figure 9, we show the output of our volume visualization of the segmented MRI.

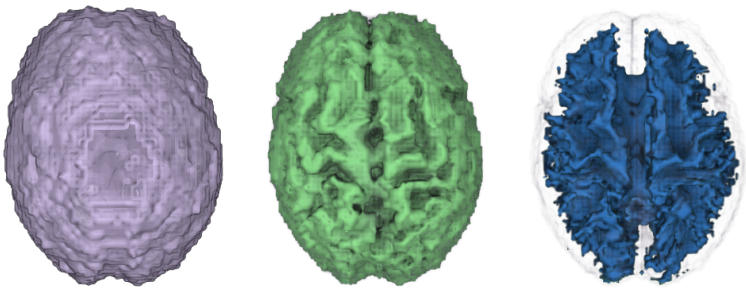

(a) (b) (c)

Fig. 9 The volume visualization of the segmented brain. The transfer function that maps the segment identifiers into color and opacity is automatically created based on segments selected by the user. In this example, the whole brain is classified into 3 segments (CSF, GM, and WM), as shown in the images.

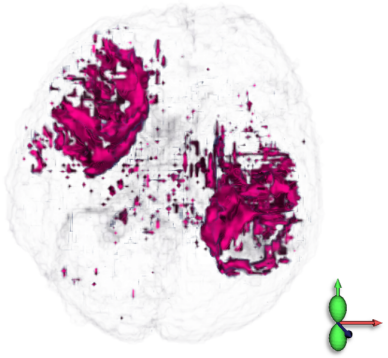

Fig. 10 The volume visualization of the spatio-angular field. Using an additional transfer function, only spatio-angular fields of selected segments are displayed. The lighting function, shown to the right of the image, is used to explore the directional strength of the spatio-angular field. As the user rotates the lighting function, a different direction is queried.

7.4 Volume Visualization of Spatio-Angular Fields

We use the framework, described in our previous work [2], to visualize spatio-angular fields and to display segmented data. In particular, we use two transfer functions. The first transfer function converts light response values to color and opacity as described in [2]. The second transfer function determines opacity based on the segments the user selects. By using both transfer functions at the same time, we allow the user to view the spatio-angular field of only the selected segments. In Figure 10, the spatio-angular field of the segment related to the injury is visualized. By rotating the lighting function (shown to the right side of the figure), users can interact with the spatio-angular field.

8 Application

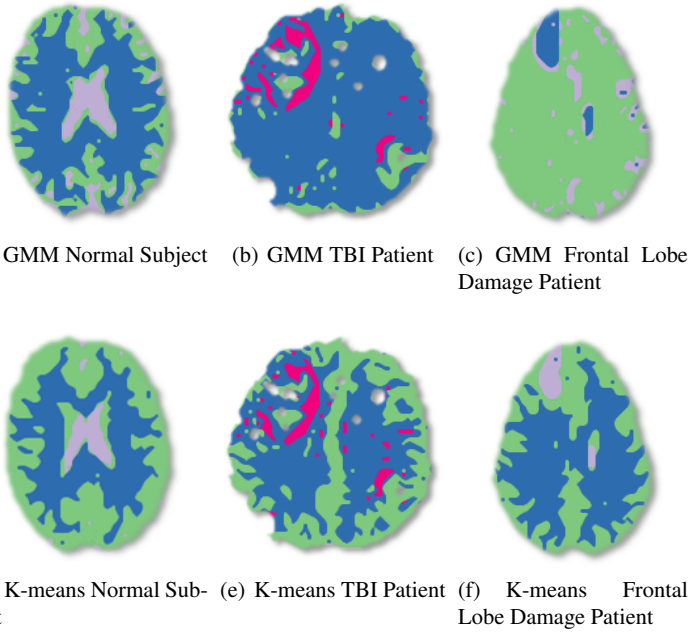

(a) GMM Normal Subject (b) GMM TBI Patient (c) GMM Frontal Lobe Damage Patient

(d) K-means Normal Subject (e) K-means TBI Patient (f) K-means Frontal Lobe Damage Patient

Fig. 11 A visual comparison between segmentation performed using domain-specific attributes and shape-based attributes. For segmentation based on domain-specific attributes, GMM is used, and for shape-based attributes, K-means is used. In the entire segmentation, we find three different segments. In Figure 11(a) and Figure 11(d), the MRI of a normal subject is used. In Figure 11(b) and Figure 11(e), the MRI of a patient suffering from TBI is shown. In Figure 11(c) and Figure 11(f), the MRI of a patient with frontal lobe damage is used. Shape-based classification captures the underlying properties of the tissues much better than segmentation created using domain-specific attributes.

8.1 Visual Comparison

We visually compare results after applying different segmentation strategies. Since GMM performed well when segmentation was based on domain-specific attributes and K-means produced the best results when shape-based attributes were used, we visually compare these two results with each other. We apply segmentation to find three segments on the MRIs of both a normal patient and a patient with an injury, as shown in Figure 11. The top row shows segmentation using domain-specific attributes, whereas the bottom row shows segmentation using shape-based attributes. Both segmentation strategies are able to distinguish basic segments, including injury. However, shape-based classification is able to capture the underlying prop-

erties of the tissues much better than segmentation done in with domain-specific attributes.

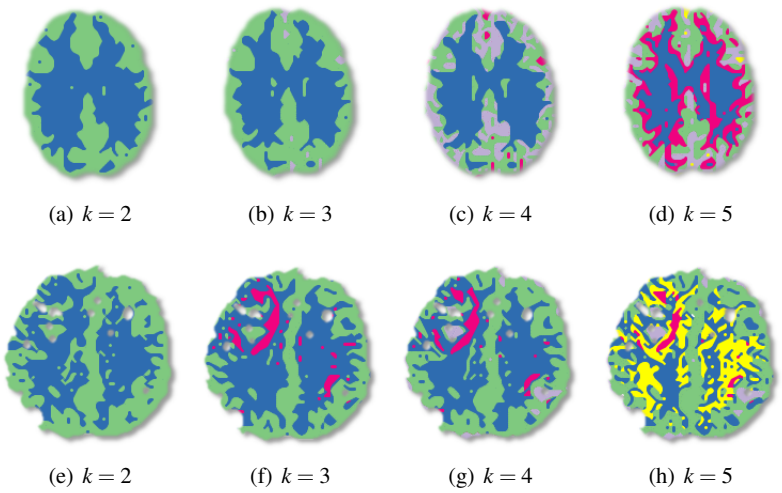

(a) $k = 2$ (b) $k = 3$ (c) $k = 4$ (d) $k = 5$

(e) $k = 2$ (f) $k = 3$ (g) $k = 4$ (h) $k = 5$

Fig. 12 A visual comparison of different segmentation strategies when the number of segments is varied for different MRI datasets. The top row uses the MRI of a normal subject and in the bottom row we use the MRI of a patient who is suffering from traumatic brain injury (TBI). Each segment in these images is colored differently. There is no relation between the coloring of segments for the normal subject and the patient suffering from traumatic brain injury.

8.2 Segment Count Variation

In classification by shape-based attributes, we tested how increasing the number of segments affects classification. In Figure 12, we show the output of segmentation using two datasets. In the MRI of the normal patient, which is shown in the top row of Figure 12, CSF, GM, and WM are clearly segmented when the number of segments is 3. As the number is further increased, subdivision within GM and CSF, occurred as seen in Figure 12(c) and Figure 12(d). In the case of the patient suffering from TBI, the region around the injury is clearly visible when the number of segments is greater than 3, as seen in Figure 12(g) and Figure 12(h).

In most of the examples of an MRI of a normal subject, we classify the entire brain into CSF, GM, and WM. For these classifications $k \leq 3$ is used. CSF, GM, and WM are structurally different; thus they have distinct diffusion profiles. In classifying a brain with an injury, we use $k \leq 4$ as we are dealing with four structurally distinct regions: CSF, GM, WM, and injury. If $k > 4$ is used, these regions are further classified. Additional study and evaluations are needed for these type of classifications.

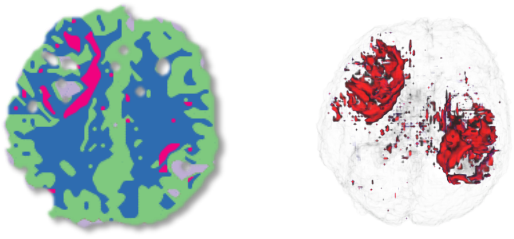

(a) Planar Visualization (b) Volume Visualization

Fig. 13 The visualization of segmentation done on the MRI of a patient suffering from a traumatic brain injury. Shape-based classification was performed using K-means segmentation (with $k = 3$) on spherical harmonics approximation of diffusion and kurtosis tensors. The segment relating to the injury is shown in red.

8.3 Traumatic Brain Injury

We apply segmentation to the MRI of a patient suffering from traumatic brain injury. We used K-means segmentation with $k = 3$ on spherical harmonics approximations of diffusion and kurtosis tensors. In Figure 13, the output of the segmentation is shown. The segmentation process is able to segment out the region around the injury (red) from other regions, such as WM (blue) and GM (green).

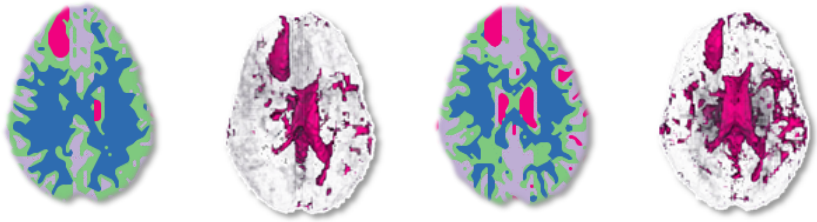

(a) (b) (c) (d)

Fig. 14 The visualization of segmentation done on the MRI of a patient with frontal lobe damage. Shape-based classification was performed using K-means segmentation (with $k = 4$) on spherical harmonics approximations of diffusion and kurtosis tensors. Figure 14(a) and Figure 14(b) are from an MRI taken 8 days after the injury. The patient showed a remarkable recovery at a one month follow-up after the injury, shown in Figure 14(c) and Figure 14(d). The red region shows an area of high diffusion, and the blue region shows white matter. The changes in the red region can be observed easily.

8.4 Frontal Lobe Injury

In the injury case shown in Figure 14, the patient has sustained frontal lobe damage. We segment the MRI dataset using K-means segmentation (with $k = 4$) on spherical harmonics approximation of diffusion and kurtosis tensors. The region in blue is associated with white matter; the region in red is related to areas with high diffusion. Right after the injury, a high diffusion region was observed in the frontal lobe, which is normally occupied by white matter, as shown in Figure 14(a) and Figure 14(b). After a month, some noticeable changes in the high diffusion region can be observed, as shown in Figure 14(c) and Figure 14(d). This aligns with the clinical diagnosis, as the patient made an significant recovery within month.

9 Conclusion And Future Work

We present a study on the classification of brain tissues using Gaussian and non-Gaussian diffusion profiles acquired from DKI. MRI classification and visualization are vital tools for medical professionals who treat patients suffering from brain diseases and injuries. The shape of both diffusion and kurtosis tensors provides important characteristics of the underlying tissues, which can be used to classify various tissue types, as shown in our study. We apply multiple segmentation strategies and compare them with the industry standard MPRAGE imaging. We also presente a way to display the segmented data effectively in planar and in volume visualization modes.

In the future, we plan to extend the utility of our tool to automatically segment various disease biomarkers in the human brain to study inflammation and neurodegeneration. We also hope to include data from other forms of imaging to further improve classification.

10 Acknowledgments

We are grateful to the anonymous reviewers whose constructive comments have greatly improved the presentation of our approach and results in this paper. We appreciate the support of the US Army grant W81XWH-12-1-0098, NSF grants 09-59979 and 14-29404, the State of Maryland's MPower initiative, and the NVIDIA CUDA Center of Excellence. Any opinions, findings, conclusions, or recommendations expressed in this article are those of the authors and do not necessarily reflect the views of the research sponsors.

References

1. J. Ashburner and K. J. Friston. Unified segmentation. Neuroimage, 26:839–851, 2005.
2. S. Bista, J. Zhuo, R. P. Gullapalli, and A. Varshney. Visualization of Brain Microstructure through Spherical Harmonics Illumination of Spatio-Angular Fields. Visualization and Computer Graphics, IEEE Transactions on, 20(12):2516–2525, Dec 2014.
3. B. Cabral, N. L. Max, and R. Springmeyer. Bidirectional reflection functions from surface bump maps. ACM Siggraph Computer Graphics, 21:273–281, 1987.
4. N. A. Carr, J. D. Hall, and J. C. Hart. GPU algorithms for radiosity and subsurface scattering. In Proceedings of the ACM SIGGRAPH/EUROGRAPHICS conference on Graphics hardware, pages 51–59. Eurographics Association, 2003.
5. Centers for Disease Control and Prevention. Traumatic Brain Injury in the United States: Fact Sheet. `www.cdc.gov/TraumaticBrainInjury/get_the_facts.html`, June 2014.
6. C. Correa and K.-L. Ma. Size-based transfer functions: A new volume exploration technique. Visualization and Computer Graphics, IEEE Trans. on, 14(6):1380–1387, 2008.
7. M. F. Falangola, J. H. Jensen, J. S. Babb, C. Hu, F. X. Castellanos, A. D. Martino, S. H. Ferris, and J. A. Helpern. Age-related non-Gaussian diffusion patterns in the prefrontal brain. Journal of Magnetic Resonance Imaging, 28:1345–1350, 2008.
8. T. Funkhouser, P. Min, M. Kazhdan, J. Chen, A. Halderman, D. Dobkin, and D. Jacobs. A search engine for 3D models. ACM Trans. on Graphics, 22(1):83–105, Jan. 2003.
9. A. Ghosh, T. Milne, and R. Deriche. Constrained diffusion kurtosis imaging using ternary quartics & mle. Magnetic Resonance in Medicine, 71(4):1581–1591, 2014.
10. X. Hao, T. Baby, and A. Varshney. Interactive subsurface scattering for translucent meshes. In ACM Symposium on Interactive 3D Graphics, pages 75 – 82, April 28 – 30, 2003.
11. J. A. Hartigan and M. A. Wong. Algorithm AS 136: A k-means clustering algorithm. Applied statistics, pages 100–108, 1979.
12. K. M. Hasan, C. Halphen, A. Sankar, T. J. Eluvathingal, L. Kramer, K. K. Stuebing, L. Ewing-Cobbs, and J. M. Fletcher. Diffusion tensor imaging-based tissue segmentation: validation and application to the developing child and adolescent brain. Neuroimage, 34(4):1497–1505, 2007.
13. R. Huang and K.-L. Ma. RGVis: Region growing based techniques for volume visualization. In Computer Graphics and Applications, 2003. Proceedings. 11th Pacific Conference on, pages 355–363. IEEE, 2003.
14. C. Y. Ip, A. Varshney, and J. JaJa. Hierarchical exploration of volumes using multilevel segmentation of the intensity-gradient histograms. Visualization and Computer Graphics, IEEE Trans. on, 18(12):2355–2363, 2012.
15. J. Jensen and J. Helpern. Quantifying non-Gaussian water diffusion by means of pulsed-field-gradient MRI. In Proceedings of the 11th Annual Meeting of ISMRM, volume 2154, 2003.
16. J. H. Jensen and J. A. Helpern. MRI quantification of non-Gaussian water diffusion by kurtosis analysis. NMR in Biomedicine, 23(7):698–710, 2010.
17. J. H. Jensen, J. A. Helpern, A. Ramani, H. Lu, and K. Kaczynski. Diffusional kurtosis imaging: The quantification of non-gaussian water diffusion by means of magnetic resonance imaging. Magnetic Resonance in Medicine, 53:1432–1440, 2005.
18. B. Jeurissen, J.-D. Tournier, T. Dhollander, A. Connelly, and J. Sijbers. Multi-tissue constrained spherical deconvolution for improved analysis of multi-shell diffusion {MRI} data. NeuroImage, (0):–, 2014.
19. D. K. Jones. Diffusion MRI theory, methods, and applications. Oxford University Press, USA, 2011.
20. J. Kautz, J. Snyder, and P.-P. J. Sloan. Fast Arbitrary BRDF Shading for Low-Frequency Lighting Using Spherical Harmonics. In Eurographics Symposium on Rendering/Eurographics Workshop on Rendering Techniques, pages 291–296, 2002.

21. M. M. Kazhdan, T. A. Funkhouser, and S. Rusinkiewicz. Rotation Invariant Spherical Harmonic Representation of 3D Shape Descriptors. In ACM International Conference Proceeding Series, pages 156–165, 2003.
22. G. L. Kindlmann and J. W. Durkin. Semi-automatic generation of transfer functions for direct volume rendering. In Volume Visualization and Graphics, pages 79–86, 1998.
23. J. Kniss, G. Kindlmann, and C. Hansen. Multidimensional transfer functions for interactive volume rendering. Visualization and Computer Graphics, IEEE Trans. on, 8(3):270–285, Jul 2002.
24. M. Lazar, J. H. Jensen, L. Xuan, and J. A. Helpern. Estimation of the orientation distribution function from diffusional kurtosis imaging. Magnetic Resonance in Medicine, 60:774–781, 2008.
25. C. H. Lee, X. Hao, and A. Varshney. Geometry-dependent lighting. IEEE Trans. on Visualization and Computer Graphics, (to appear), 2005.
26. C. H. Lee, Y. Kim, and A. Varshney. Saliency-guided lighting. IEICE Trans. on Information and Systems, E92-D(2):369 – 373, February 2009.
27. M. Levoy. Display of surfaces from volume data. IEEE Computer Graphics and Applications, 8:29–37, 1988.
28. T. Liu, H. Li, K. Wong, A. Tarokh, L. Guo, and S. T. Wong. Brain tissue segmentation based on dti data. NeuroImage, 38(1):114–123, 2007.
29. H. Lu, J. H. Jensen, A. Ramani, and J. A. Helpern. Three-dimensional characterization of non-gaussian water diffusion in humans using diffusion kurtosis imaging. NMR in Biomedicine, 19(2):236–247, 2006.
30. E. B. Lum and K.-L. Ma. Lighting transfer functions using gradient aligned sampling. In Proceedings of the conference on Visualization'04, pages 289–296. IEEE Computer Society, 2004.
31. G. McLachlan and D. Peel. Finite mixture models. John Wiley & Sons, 2004.
32. M. J. Mohlenkamp. A Fast Transform for Spherical Harmonics. Journal of Fourier Analysis and Applications, 1997.
33. V. Prckovska, T. H. J. M. Peeters, M. Van Almsick, B. ter Haar Romeny, and A. Vilanova i Bartroli. Fused DTI/HARDI Visualization. Visualization and Computer Graphics, IEEE Trans. on, 17(10):1407–1419, 2011.
34. V. Prkovska, A. Vilanova, C. Poupon, B. Haar Romeny, and M. Descoteaux. Fast Classification Scheme for HARDI Data Simplification. In D. Davcev and J. Gómez, editors, ICT Innovations 2009, pages 345–355. Springer Berlin Heidelberg, 2010.
35. T. Roine, B. Jeurissen, D. Perrone, J. Aelterman, A. Leemans, W. Philips, and J. Sijbers. Isotropic non-white matter partial volume effects in constrained spherical deconvolution. Frontiers in Neuroinformatics, 8(28):1–9, 03/2014 2014.
36. P. Schlegel, M. Makhinya, and R. Pajarola. Extinction-Based Shading and Illumination in GPU Volume Ray-Casting. IEEE Trans. on Visualization and Computer Graphics, 17(12):1795–1802, 2011.
37. F. X. Sillion, J. R. Arvo, S. H. Westin, and D. P. Greenberg. A global illumination solution for general reflectance distributions. In ACM SIGGRAPH Computer Graphics, volume 25, pages 187–196. ACM, 1991.
38. P.-P. Sloan, J. Kautz, and J. Snyder. Precomputed radiance transfer for real-time rendering in dynamic, low-frequency lighting environments. In ACM Trans. on Graphics (TOG), volume 21, pages 527–536. ACM, 2002.
39. Y. Tao, H. Lin, H. Bao, F. Dong, and G. Clapworthy. Structure-aware viewpoint selection for volume visualization. In Visualization Symposium, Pacific Asia-Pacific, pages 193–200, 2009.
40. C. M. Tax, W. M. Otte, M. A. Viergever, R. M. Dijkhuizen, and A. Leemans. Rekindle: Robust extraction of kurtosis indices with linear estimation. Magnetic Resonance in Medicine, 2014.
41. A. Tikhonova, C. D. Correa, and K.-L. Ma. An exploratory technique for coherent visualization of time-varying volume data. Computer Graphics Forum, 29(3):783–792, 2010.
42. Y. Zhang and K.-L. Ma. Lighting Design for Globally Illuminated Volume Rendering. Visualization and Computer Graphics, IEEE Trans. on, 19(12):2946–2955, 2013.

43. J. Zhuo, S. Xu, J. L. Proctor, R. J. Mullins, J. Z. Simon, G. Fiskum, and R. P. Gullapalli. Diffusion kurtosis as an in vivo imaging marker for reactive astrogliosis in traumatic brain injury. NeuroImage, 59(1):467 – 477, 2012.

Index